

The MICE Grand Challenge Lightcone Simulation I: Dark matter clustering

P. Fosalba^{*}, M. Crocce, E. Gaztañaga, & F. J. Castander

Institut de Ciències de l’Espai, IEEC-CSIC, Campus UAB, Facultat de Ciències, Torre C5 par-2, Barcelona 08193, Spain

^{*} Dedicated to my mother, Florencia

30 July 2015

ABSTRACT

We present a new N-body simulation from the MICE collaboration, *the MICE Grand Challenge* (MICE-GC), containing about 70 billion dark-matter particles in a $(3Gpc/h)^3$ comoving volume. Given its large volume and fine spatial resolution, spanning over 5 orders of magnitude in dynamic range, it allows an accurate modeling of the growth of structure in the universe from the linear through the highly non-linear regime of gravitational clustering. We validate the dark-matter simulation outputs using 3D and 2D clustering statistics, and discuss mass-resolution effects in the non-linear regime by comparing to previous simulations and the latest numerical fits. We show that the MICE-GC run allows for a measurement of the BAO feature with percent level accuracy and compare it to state-of-the-art theoretical models. We also use sub-arcmin resolution pixelized 2D maps of the dark-matter counts in the lightcone to make tomographic analyses in real and redshift space. Our analysis shows the simulation reproduces the Kaiser effect on large scales, whereas we find a significant suppression of power on non-linear scales relative to the real space clustering. We complete our validation by presenting an analysis of the 3-point correlation function in this and previous MICE simulations, finding further evidence for mass-resolution effects. This is the first of a series of three papers in which we present the MICE-GC simulation, along with a wide and deep mock galaxy catalog built from it. This mock is made publicly available through a dedicated webportal, <http://cosmohub.pic.es>.

Key words: methods: numerical,(cosmology):large-scale structure of Universe, (cosmology):dark matter,galaxies: statistics

1 INTRODUCTION

These are exciting times for cosmology. The new generation of astronomical surveys will deliver a detailed picture of the universe, providing a better understanding of the galaxy formation process and determining whether General Relativity correctly describes the observables that characterize the expansion rate of the universe and the growth of large-scale structures. In particular one of the main science goals of upcoming galaxy surveys is to pin down the properties of the dark-energy that drives the observed accelerated expansion of the universe.

In order to answer these key questions we need to interpret astronomical datasets with high precision. Given the difficulty of the problem, N-body simulations have become a fundamental ingredient to develop mock cosmological observations, by providing a laboratory for the growth of structure under the only effect of gravity. However, the ever increasing volume and complexity of observational datasets demands a matching effort to develop larger and higher accuracy cosmological simulations.

In this paper we present a new N-body simulation developed by the Marenostrum Institut de Ciències de l’Espai (MICE) collaboration at the Marenostrum supercomputer,

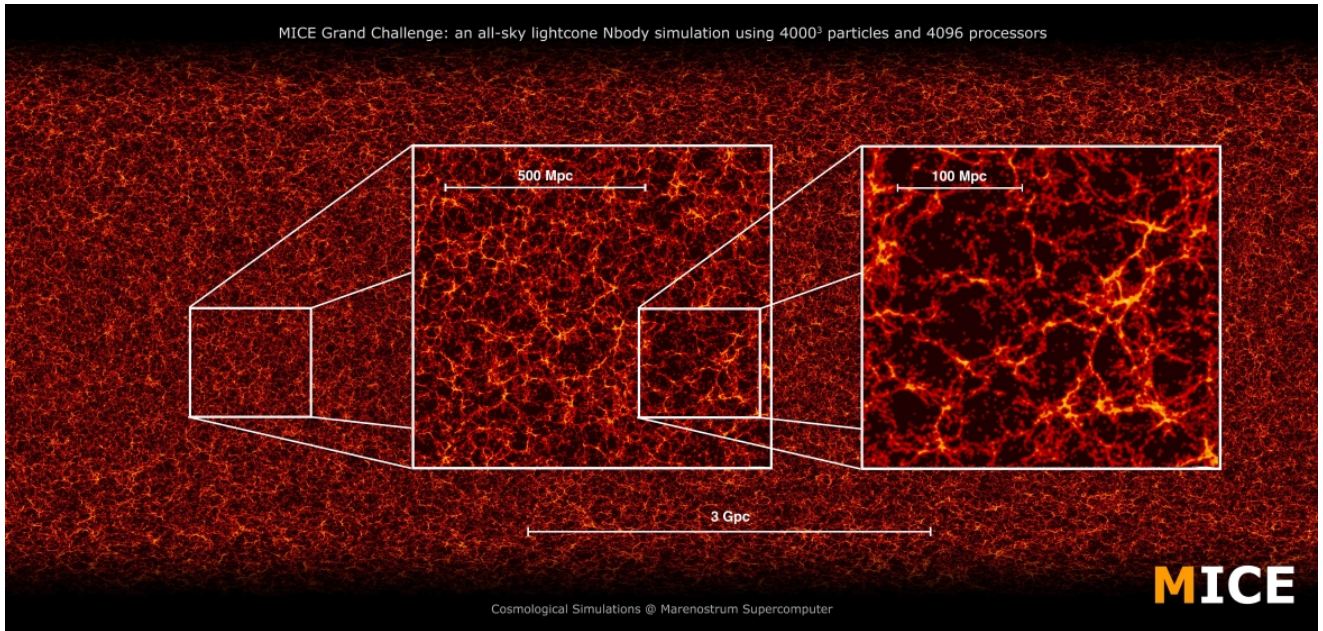


Figure 1. MICE-GC dark-matter lightcone simulation at $z = 0.6$. The image shows the wide dynamic range, about 5 decades in scale, sampled by this Nbody simulation.

the MICE *Grand Challenge* run (MICE-GC), that includes about 70 billion dark-matter particles, in a box of about $3 h^{-1}$ Gpc aside. This simulation samples from the largest (linear) scales accessible to the observable universe, where clustering statistics are Gaussian, down to to the highly non-linear regime of structure formation where gravity drives dark-matter and galaxy clustering away from Gaussianity. We build halo and galaxy catalogues in order to help the design and exploitation of new wide-area cosmological surveys. We present several applications of this large cosmological simulation for 2D and 3D clustering statistics of dark-matter in comoving outputs and in the lightcone.

One of the main focus of this paper is to investigate the impact of *mass-resolution effects* in the modeling of dark-matter and galaxy clustering observables by comparing the MICE-GC, and previous MICE runs, to analytic fits available based on high-resolution N-body simulations. For this purpose, we have thoroughly analyzed the simulation outputs using basic 3D and 2D clustering statistics in comoving outputs and in the lightcone. We show that our results are consistent with previous work in linear and weakly non-linear scales, and show how the new simulation better samples power on small-scales, described by the highly non-linear regime of gravitational clustering.

This paper is the first of a series of three introducing the MICE-GC end-to-end simulation, its validation and several applications. Paper I (i.e. this paper) presents the MICE-GC N-body lightcone simulation and its validation using dark-matter clustering statistics. The halo and mock galaxy catalog, along with their validation and applications

to abundance and clustering statistics are presented in Paper II (Crocco et al. 2013). The all-sky lensing maps and the inclusion of lensing properties to the mock galaxies are discussed in Paper III (Fosalba et al. 2015).

Accompanying this series of papers, we make a first public data release of the MICE-GC lightcone galaxy mock (MICECAT v1.0) through a dedicated web-portal for simulations: <http://cosmohub.pic.es>, where detailed information on the data provided can be found. We plan to release improved versions of the MICE galaxy mocks through this web-portal in due time.

This paper is organized as follows: Section §2 presents the MICE-GC simulation and how it compares to state-of-the-art in the field of numerical simulations in cosmology. In §3, we validate the dark-matter outputs of the simulation using the 3D matter power-spectrum, and its Fourier transform, the 2-point correlation function (i.e., 2PCF). In §4 we investigate the distribution of dark-matter in the all-sky lightcone by means of 2D pixelized maps. We focus in the clustering of projected dark-matter counts in redshift bins in real and redshift space using the angular power spectrum and its Legendre Transform, the angular 2PCF. We compare these results to previous simulations and available numerical fits. Section §5 presents an analysis of the 3-point correlation function of the dark-matter comoving outputs in the MICE-GC, and compares it to previous MICE runs and theory predictions. Finally, in §6 we summarize our main results and conclusions.

Run	N_{part}	L_{box}/h^{-1} Mpc	$PMGrid$	$m_p/(10^{10} h^{-1} M_{\odot})$	l_{soft}/h^{-1} Kpc	z_i	$Max.TimeStep$
MICE-GC	4096^3	3072	4096	2.93	50	100	0.02
MICE-IR	2048^3	3072	2048	23.42	50	50	0.01
MICE-SHV	2048^3	7680	2048	366	50	150	0.03

Table 1. Description of the MICE N-body simulations. N_{part} denotes number of particles, L_{box} is the box-size, $PMGrid$ gives the size of the Particle-Mesh grid used for the large-scale forces computed with FFTs, m_p gives the particle mass, l_{soft} is the softening length, and z_{in} is the initial redshift of the simulation. All simulations had initial conditions generated using the Zeldovich Approximation. Max. Time-step is the initial global time-stepping used, which is of order 1% of the Hubble time (i.e, $d \log a = 0.01$, being a the scale factor). The number of global time-steps to complete the runs were $N_{\text{steps}} \gtrsim 2000$ in all cases, except for the MICE-GC which took $\gtrsim 3000$ time-steps. Their cosmological parameters were kept constant throughout the runs (see text for details).

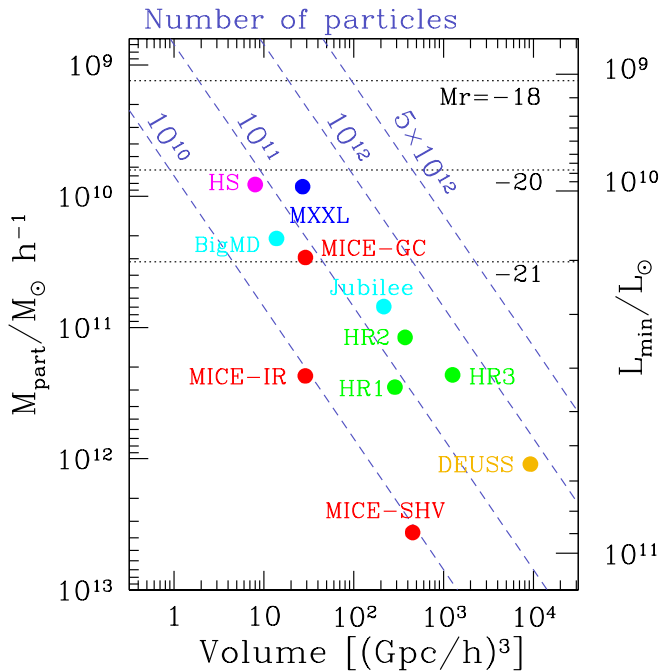


Figure 2. State-of-the art in cosmological simulations: performance in terms of survey volume and particle mass, or equivalently, faintest L_{min} galaxy luminosity (or absolute magnitude in r-band) reached according to an HOD galaxy assignment scheme to populate halos with 100 or more dark-matter particles.

2 THE MICE GRAND CHALLENGE SIMULATION

We have developed a set of large N-body simulations with Gadget-2 (Springel 2005) on the Marenostrum supercomputer at BSC¹. We shall name them MICE (MareNostrum - Instituto de Ciencias del Espacio) simulations hereafter. Further details about the MICE simulations can be found in the project website, www.ice.cat/mice.

In this paper we shall focus on the MICE *Grand Chal-*

lenge simulation (MICE-GC hereafter). This simulation contains 4096^3 dark-matter particles in a box-size of $L_{\text{box}} = 3072 h^{-1}$ Mpc, and assumes a flat concordance LCDM model with $\Omega_m = 0.25$, $\Omega_{\Lambda} = 0.75$, $\Omega_b = 0.044$, $n_s = 0.95$, $\sigma_8 = 0.8$ and $h = 0.7$, consistent with the best-fit cosmology to WMAP 5-year data Dunkley et al. (2009). The resulting particle mass is $m_p = 2.93 \times 10^{10} h^{-1} M_{\odot}$ and the softening length used is, $l_{\text{soft}} = 50 \text{ kpc}/h$. We start our run at $z_i = 100$ displacing particles using the Zeldovich dynamics. The initial particle load uses a cubic mesh with 4096^3 nodes. The entry Max. Time-step in Table 1 is the initial global time-stepping used, which is of order 1% of the Hubble time (i.e, $d \log a = 0.01$, being a the scale factor). The number of global time-steps to complete the run was $N_{\text{steps}} \gtrsim 3000$, and we write the lightcone on-the-fly in 265 steps from $z=1.4$ to $z=0$.

In Table 1 we describe the Gadget-2 code parameters used in the MICE simulations discussed in this paper: the MICE Grand-Challenge (MICE-GC), the Intermediate Resolution (MICE-IR; Fosalba et al. (2008)) and the Super-Hubble Volume (MICE-SHV; Crocce et al. (2010)).

We construct a lightcone simulation by replicating the simulation box (and translating it) around the observer, thus allowing to build all-sky lensing outputs with negligible repetition up to $z_{\text{max}} = 1.4$. The methodology used to develop all-sky (spherical) lightcone outputs is described in (Fosalba et al. 2008), where further details are given on how the all-sky lensing maps in the Born approximation are constructed using pixelized 2D projected dark-matter density maps. Figure 1 shows an image of the all-sky lightcone at $z = 0.6$. The nested zooms illustrate the wide dynamic range sampled by the simulation. In particular, thanks to its combination of large volume and good mass resolution, the MICE-GC simulation is able to sample from the largest (linear) scales encompassing nearly all the observable universe down to fairly small (non-linear) scales with few percent accuracy, as we shall show in this work.

A particularly challenging aspect of any large-volume cosmological simulation is the ability to accurately sample small-scale (non-linear) power while still sampling a large

¹ Barcelona Supercomputing Center, www.bsc.es

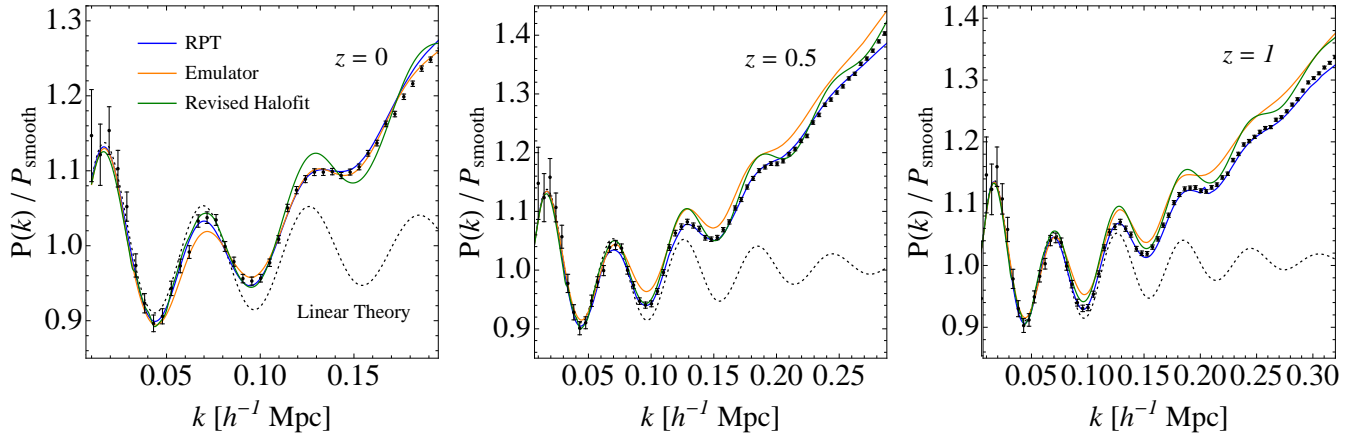


Figure 3. Baryon Acoustic Oscillations (BAO) measured in MICE-GC (black symbols with error-bars) power spectrum compared to the theory prediction from Renormalized Perturbation Theory, RPT (blue line, see Crocce and Scoccimarro 2008) and the latest numerical fit from the Coyote Emulator (orange line, Heitmann et al. 2013) and the revised Halofit (green line, Takahashi et al. 2012). The RPT model at two loops reproduces very well the BAO in the simulation across redshifts (each panel is shown up to the maximum k where RPT is valid). In turn at $z = 0$ the Emulator yields a very good match with MICE-GC (except for the amplitude of the first peak with a difference $\lesssim 2\%$). At $z = 0.5, 1$ the broad-band power has the correct shape but is 2% (systematically) above the N-body. The revised halofit also agrees with MICE-GC at the 2% level at these redshifts but the amplitude of the oscillations are somewhat too large. Displayed error-bars assume Gaussian fluctuations, $\sigma_P = \sqrt{2/n_{\text{modes}}P_k}$, but we take P_k to be the non-linear spectrum (see text).

volume. This ability is determined by the particle mass (or density of particles) in the simulated volume. In what follows, we shall refer to the impact of the particle mass on clustering observables as *mass-resolution effects*.

In this paper we introduce this new very large cosmological simulation as a powerful tool to model accurately current and upcoming deep wide-area astronomical surveys such as DES², HSC³, Euclid⁴, DESI⁵, HETDEX⁶, LSST⁷, WFIRST⁸, among others.

We test the ability of MICE-GC to model these large-surveys on the smaller scales and to what extent it resolves the small-mass halos inhabited by the faintest galaxies these surveys will observe. Figure 2 shows how MICE-GC compares to the largest simulations currently available in performance to sample large cosmological volumes and capture, at the same time, low enough luminosity galaxies L_{min} , or equivalently, large enough r-band absolute magnitude M_r . The relation between minimum halo mass and minimum galaxy luminosities modeled, as shown in the Figure, assumes a sub-halo abundance matching galaxy assignment scheme on well-resolved dark-matter halos containing at least 100 particles. We show the following simulations: Millennium XXL (MXXL; Angulo et al. (2012)), Horizon Runs (HR; Kim et al. (2009, 2011)), Horizon Simulation (HS;

Teyssier et al. (2009)), DEUSS (Alimi et al. 2012), Jubilee (Watson et al. 2013), BigMultiDark(Klypin et al. 2013), MICE Intermediate Resolution (MICE-IR; Fosalba et al. (2008)), MICE Super-Hubble-Volume (MICE-SHV; Crocce et al. (2010)) and the MICE-GC simulation.

This suite of simulations includes numbers of particles that span from about 10 billion up to 1 trillion particles, already accesible in the largest supercomputers around the world. This figure shows the trade-off between high mass resolution and large volume sampling what tends to distribute the most competitive simulations to date along the dashed lines shown, depending on the number of particles used. As shown in Fig. 2, the MXXL is the state-of-the art cosmological simulation in terms of sampling as large a volume as possible with a high mass resolution. Our simulation compares well to it, as it has a comparable volume (3.072 Gpc/h) and only 4 times lower mass resolution ($2.93 \times 10^{10} h^{-1} M_{\odot}$).

As an example, in order to resolve $M_r = -18$ galaxies one would need to develop a simulation with a $(4 \text{ Gpc/h})^3$ box-size that includes about 5 trillion particles (i.e, 16384^3). This is one order of magnitude larger than the MXXL and almost two orders of magnitude bigger than e.g, the MICE-GC, which are among the largest simulations completed to date.

3 3D CLUSTERING

3.1 Power spectrum

One of our main goals is to study the large scale clustering with high precision, in particular the baryon acoustic oscilla-

² www.darkenergysurvey.org

³ www.naoj.org/Projects/HSC

⁴ www.euclid-ec.org

⁵ desi.lbl.gov

⁶ hetdex.org

⁷ www.lsst.org

⁸ wfirst.gsfc.nasa.gov

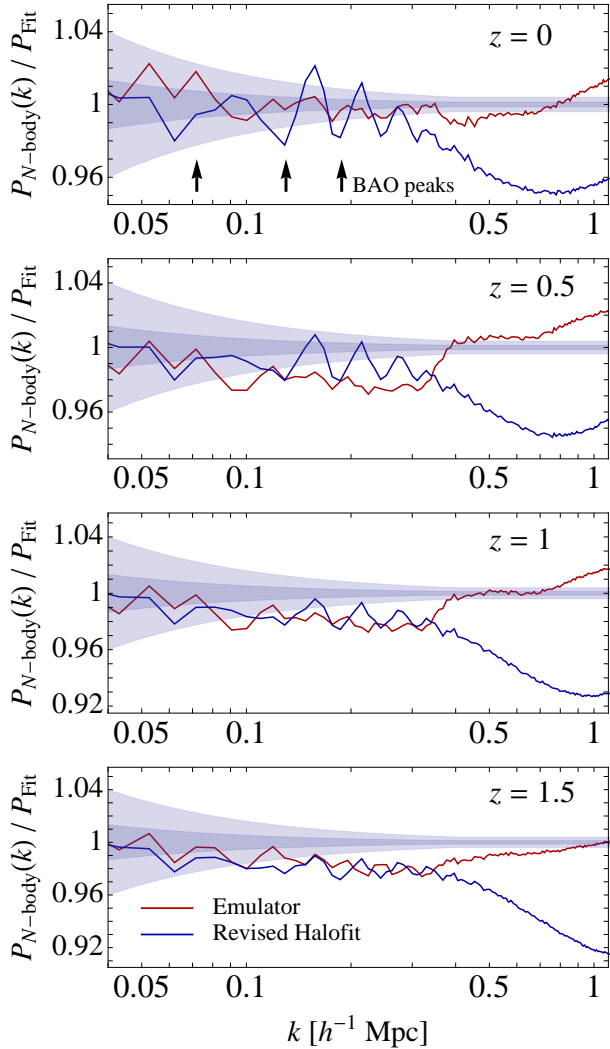


Figure 4. Matter power spectrum in MICE-GC at several comoving outputs compared to the latest available numerical fits, the revised Halofit (Takahashi et al. 2012) and the Coyote Emulator (Heitmann et al. 2013). The shaded regions show the $1 - \sigma$ and $3 - \sigma$ error bars given the box-size and the binning (see text for details). The overall matching with the emulator is at the level of 2% (but systematically below), with a jump of $\lesssim 3\%$ at $k \sim 0.3 - 0.4 h^{-1} \text{Mpc}$. In turn, the revised Halofit over-predicts the power on small scales by 5% to 8% (see text for a more detailed discussion). Vertical arrows show BAO peaks for reference.

tions (BAO). Hence Fig. 3 shows the matter 3D power spectrum measured in MICE-GC at large (BAO) scales for three comoving outputs, $z = 0, 0.5$ and 1 (divided by a smooth broad-band power). For comparison we included linear theory, the Renormalized Perturbation Theory prediction as presented in Crocce & Scoccimarro (2008), and the numerical fits from Heitmann et al. (2013) (i.e., the Coyote Emulator) and Takahashi et al. (2012), which we shall name the *revised halofit*. The prediction from RPT at two-loops reproduces very well the region of BAO, thus cross validating

the modeling and the N-body precision in describing this feature. We find the Coyote Emulator to give a good description of the overall BAO features in our run, but with a systematic 2% excess (broad-band) amplitude at $z = 0.5, 1$. The revised Halofit yields a similar level of agreement but in that case the amplitude of the oscillatory features appear too large.

In Fig. 3 displayed error bars corresponds to the FKP formula (Feldman et al. 1994):

$$\sigma_P = \sqrt{\frac{2}{n_{\text{modes}}}} P \quad (1)$$

but using P as the non-linear power spectrum (and no shot-noise, as this is negligible for MICE-GC). In Eq. 1 $n_{\text{modes}} = 4\pi \delta k k_f$ is the number of modes, $k_f = 2\pi/L_{\text{box}}$ the fundamental mode for the given boxsize, and δk the bin width in k -space. We have tested that this yields a good estimate for the statistical errors at BAO scales with an independent ensemble of simulations (Crocce & Scoccimarro 2008). Similar conclusions are found in Angulo et al. (2008). At $k \geq 0.4 h^{-1} \text{Mpc}$ we find that the relative error σ_P/P flattens out to a roughly constant value (see also Takahashi et al. (2009); Smith (2009)).

In turn, Fig. 4 shows the MICE-GC 2-pt clustering measurements in the transition to the highly nonlinear regime and how they compare to the revised Halofit and the Coyote Emulator on those scales⁹. Different panels correspond to different comoving outputs, namely $z = 0, 0.5, 1$ and 1.5 (top to bottom). As discussed above the Emulator is systematically above our measurement on scales $k \lesssim 0.3 h \text{Mpc}^{-1}$ by about 2% (for $z > 0$). Towards smaller scales we find a pronounced jump in the prediction at intermediate redshifts and $k \sim 0.3 - 0.4 h \text{Mpc}^{-1}$ of $\sim 3\%$. The overall matching with MICE-GC measurements stays at the level of $\pm 2\%$ up to $k \sim 1 h \text{Mpc}^{-1}$. The revised Halofit is slightly above our measurements across scales, but particularly at the “one-halo” regime beyond $k \sim 0.3 h \text{Mpc}^{-1}$, where differences rise to about 5–8% depending on redshift. In Fig. 4, and following the discussion after Eq. (1), we display 1 and 3σ error bars with shaded regions using Eq. (1) for $k \leq 0.4 h \text{Mpc}^{-1}$ and its value $(\sigma_P/P)|_{k=0.4}$ for $k \geq 0.4 h \text{Mpc}^{-1}$.

We should note that on small scales ($k \sim 1 h \text{Mpc}^{-1}$) our run might suffer from percent level systematics effects that could impact the discussion above. For example setting the size of the Particle-Mesh grid (the PMGrid parameter) equal to the number of particles (as done in MICE-GC, see Table 1), instead of larger, can yield excess power on quasi-linear scales of $\lesssim 1\%$ (Smith et al. 2012). In turn, transients

⁹ We restrict the comparison to scales ($k \sim 1 h \text{Mpc}^{-1}$) where shot-noise in MICE-GC is negligible. In addition the power spectrum estimation was done using a CIC assignment scheme with a large mesh ($k_{\text{Ny}} = 2 h \text{Mpc}^{-1}$) which, after correction from the FT of the assignment function, is sufficient to avoid aliasing effects on the scales of interest.

from initial conditions suppress power on these scales. For MICE-GC, with $z_i = 100$, we expect this to be a small effect nonetheless. For an order of magnitude we have estimated the relative transient effect (i.e. $P(k, z_i = 100)/P(k, z_i = \infty)$) using perturbation theory (PT, see Fig. 6 in Crocce et al. (2006)) and found a $\sim (1 - 1.5)\%$ effect at scales $k \sim 0.5 - 1 h \text{ Mpc}^{-1}$.

We next turn to discuss the impact of particle mass resolution in the generation of nonlinear structure by comparing the clustering in MICE-GC to that in MICE-IR, a factor of 8 worse resolution run. This lower resolution simulation was already presented and extensively validated in Fosalba et al. (2008), and Crocce et al. (2010)¹⁰. We note that both simulations were done with almost the same run parameters (see Table 1) with the main difference being the initial transfer function. MICE-IR used the Eisenstein & Hu (EH from now on) approximation (Eisenstein & Hu 1998) while MICE-GC used an (exact) CAMB output¹¹. The differences between these two initial spectra, shown in the top panel of Fig. 5, are however very small: $\lesssim 4\%$ at BAO positions and within 2% up to $k \sim 50 h \text{ Mpc}^{-1}$ (although only $k < 1 h \text{ Mpc}^{-1}$ is plotted).

The resolution study is given in the bottom panel of Fig. 5. It shows that the nonlinear power spectrum measured in MICE-IR is suppressed compared to that in MICE-GC, by 3%, 5% and $\sim 8\%$ at $k = 1 h \text{ Mpc}^{-1}$ and $z = 0, 0.5$ and 1 respectively. These differences are somewhat expected because particle mass resolution impacts how well small-scale power is sampled from the simulated dark-matter distribution. The lower the particle mass, the better small scales are sampled. In the language of the halo model, a smaller particle mass is able to resolve smaller-mass halos that contribute to the power spectrum on correspondingly smaller scales. Notice that the effect can be significant even on rather large-scales (1% to 2% at $k \sim 0.4 h \text{ Mpc}^{-1}$). In Fig. 5 the MICE-IR power spectra have been corrected for finite particle number assuming a Poisson shot-noise (while MICE-GC has negligible noise on these scales). If we have not done so the $P(k)$ ratio at different redshifts would have resembled the $z = 0$ case in Fig. 5, i.e. a resolution effect being $\sim 2\% - 3\%$ at $k = 1 h \text{ Mpc}^{-1}$. One difference between the simulation runs that can impact part of the effect shown in Fig. 5 is the starting redshift. Because MICE-IR started at a lower redshift than MICE-GC ($z_i = 50$ vs. $z_i = 100$, respectively) its clustering is expected to be suppressed at non-linear scales. However we have estimated this to be a 1% effect in the k -range $0.5 - 1 h \text{ Mpc}^{-1}$ for the redshifts shown (using PT, see Crocce et al. (2006)).

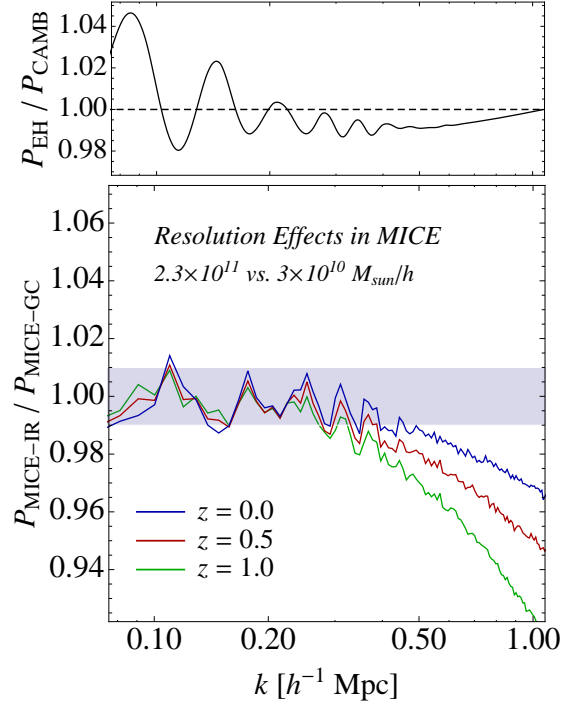


Figure 5. TOP PANEL: Ratio of the initial Eisenstein & Hu linear power spectrum used in MICE-IR to the one used in MICE-GC from CAMB, both for the same (MICE) cosmology. BOTTOM PANEL: suppression of nonlinear structure formation due to particle mass resolution seen through the ratio of the power spectrum measured in MICE-IR ($m_p \sim 2.3 \times 10^{11} h^{-1} M_{\odot}$) to the one in MICE-GC ($m_p \sim 3 \times 10^{10} h^{-1} M_{\odot}$) at $z = 0, 0.5$ and 1. MICE-IR measurements were corrected assuming a Poisson shot-noise and the slight difference in initial spectra was divided out. If we do not correct for shot-noise we find these ratios to be almost independent of redshift and to resemble the $z = 0$ case shown by the blue line.

3.2 2-point correlation function

To complement the previous sections we show in left panel of Fig. 6 the spatial correlation function of dark matter particles in the $z = 0$ comoving output of MICE-GC. This is basically the Fourier counterpart of Fig. 3 but it is still interesting to see how any mismatch between the measurements and the theory in that figure translate to configuration space. The BAO wiggles from the revised Halofit (Takahashi et al. 2012) which are too pronounced in Fourier Space also yield the wrong amplitude for the correlation turn-over at $\sim 90 h^{-1} \text{ Mpc}$ and the BAO peak at $110 h^{-1} \text{ Mpc}$. Both RPT (Crocce & Scoccimarro 2008) and Coyote (Heitmann et al. 2013) seem to agree better with MICE-GC. All models agree very well with themselves and the measurements on smaller scales, $20 h^{-1} \text{ Mpc} \leq r \leq 70 h^{-1} \text{ Mpc}$. For concreteness we focused on $z = 0.5$ but similar conclusions are reached for $z = 0$ and $z = 1$.

Right panel of Fig.6, shows the correlation function measurements for different redshifts in the lightcone. The top-hat filter is a cubical cell of side $8 \text{ Mpc}/h$. We split the

¹⁰ note that in Crocce et al. 2010, the MICE-IR simulation was named MICE3072, see their Table 1 for details

¹¹ <http://camb.info/>

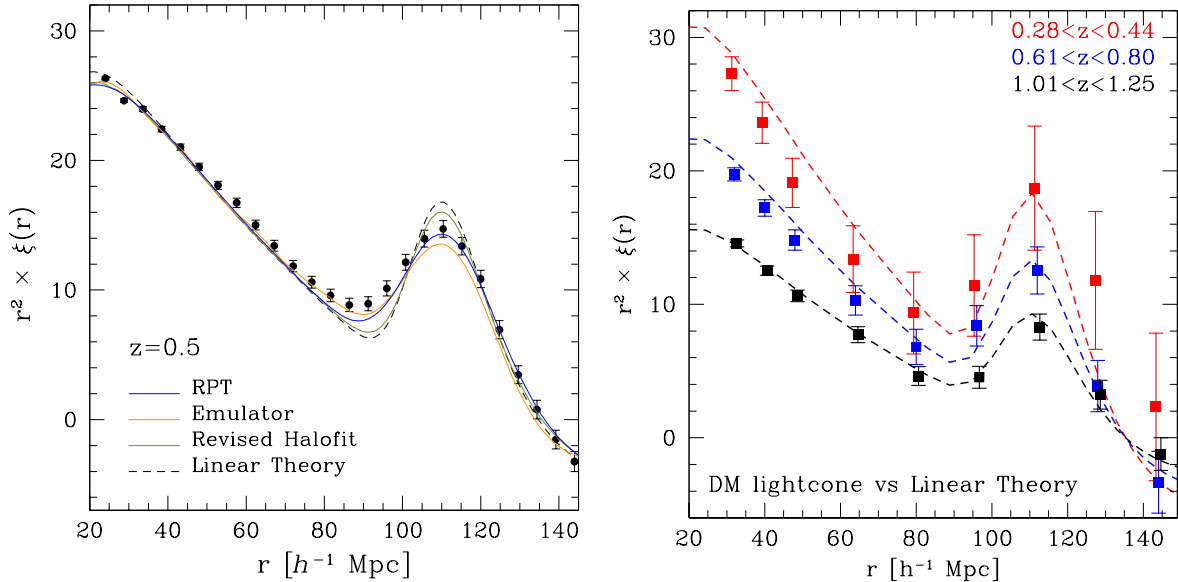


Figure 6. LEFT PANEL: Dark-matter correlation function in MICE-GC at $z = 0.5$ at large-scales (the Fourier counterpart to the middle panel of Fig. 3). We include the Fourier transform of the models shown in Fig 3: RPT (blue, Crocce and Scoccimarro 2008), Emulator (orange, Heitmann et al. 2013), the revised Halofit (green, Takahashi et al. 2012) and linear theory (dashed black). The later is the one that shows the worse agreement with our N-body at BAO scales (in the amplitude of the feature), while RPT and Emulator are in better agreement. Similar conclusions are reached at $z = 0$ and 1. RIGHT PANEL: Corresponding results for difference redshift slices over one octant of the MICE-GC lightcone output (also in real space) smoothed over $8 h^{-1}$ Mpc pixels and $16 h^{-1}$ Mpc bins in pair separation r . Dashed lines are the smoothed linear theory predictions (which resemble non-linear predictions). Note how the errors are larger (and more realistic) because of the smaller volume available in the lightcone.

correlation in bins of 16 Mpc/h to reduce the errorbars. So the smoothing is not necessary, but it speeds up the codes, which are the same we use for the 3-pt correlation, for which the execution time reduction is critical. The redshift bin is given in complete cell sizes which also reduces the impact of the boundaries. The redshifts depth could add some effects due to selection in redshift space, but we have checked that mean results do not change much (within errors) for other bin widths. This smoothing makes the linear and non-linear results look quite closer on BAO scales. On the largest scales there is good agreement, within the errors, with the linear theory predictions (dashed lines), specially at the larger redshifts. At the lower redshifts, non-linear effects are more important (distorting the shape of the BAO peak and the amplitude around $r \simeq 40 - 80 h^{-1}$ Mpc) and errors are larger because of the smaller volume in the lightcone. Given these errors and the smoothing, it is hard to evaluate if there are additional lightcone distortions in addition to the non-linear effects that we find in the comoving outputs.

4 ANGULAR CLUSTERING IN THE LIGHTCONE

Following the approach presented in Fosalba et al. (2008), we construct a lightcone simulation by replicating the sim-

ulation box (and translating it) around the observer. Given the large box-size used for the MICE-GC simulation, $L_{box} = 3072 h^{-1}$ Mpc, this approach allows us to build all-sky lightcone outputs without significant repetition up to $z_{max} = 1.4$. Then we decompose the lightcone volume, in the range $0 < z < 1.4$, into a set of 265 all-sky concentric spherical (or radial) shells around the observer, with a constant width of ~ 70 Mega-years in lookback time. This width corresponds to about 8 Mpc/h at $z \simeq 0$ and 15 Mpc/h at $z \simeq 1.4$. Lightcone outputs are written on the fly for each of these spherical shells. We linearly interpolate particle positions using their velocities at the lightcone timestep or radial shell.

4.1 Angular Clustering in Real Space

Next we validate our simulation dark-matter outputs in 2D. In order to do this we use the all-sky 3D lightcone dark-matter density, decomposed into narrow spherical redshift slices, and projected onto 2D pixelized maps using the Healpix tessellation¹² (Górski et al. 2005). As a first statistical test, we compare the 2-point statistics to theoretical predictions. In general, one defines the angular power spectra of scalar

¹² <http://sourceforge.net/projects/healpix>

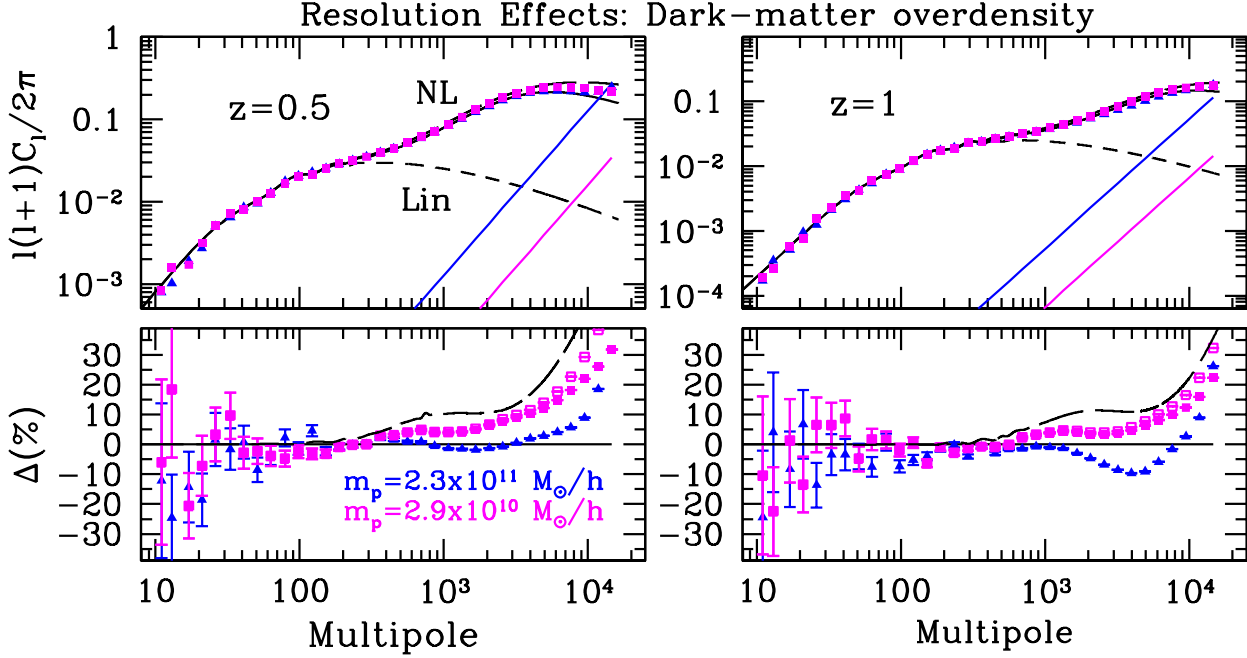


Figure 7. Angular power spectrum of the projected dark-matter overdensity field in redshift (all-sky lightcone) slices. Left panels show power spectra for a broad z -bin slice at $z = 0.5$ and $\Delta z = 0.1$, whereas the right panels show the case for $z = 1$ with the same binwidth. Dashed and solid lines show linear theory and non-linear fit (Halofit) predictions, respectively. Long dashed lines shows the *revised Halofit* (Takahashi et al. 2012) which shows a clear excess of power with respect to the *old Halofit* (Smith et al. 2003). Symbols show measurements from simulations and the solid lines at the bottom right display the estimated shot-noise levels. Lower panels show relative deviations with respect to the the old Halofit prediction. For clarity, in these lower panels, we only show power spectra both with (open symbols) and without (filled symbols) shot-noise for the MICE-GC simulation, where shot-noise does not affect small-scale power significantly. Mass resolution effects at the 20 – 30% level are observed for multipoles $\ell > 10^3$.

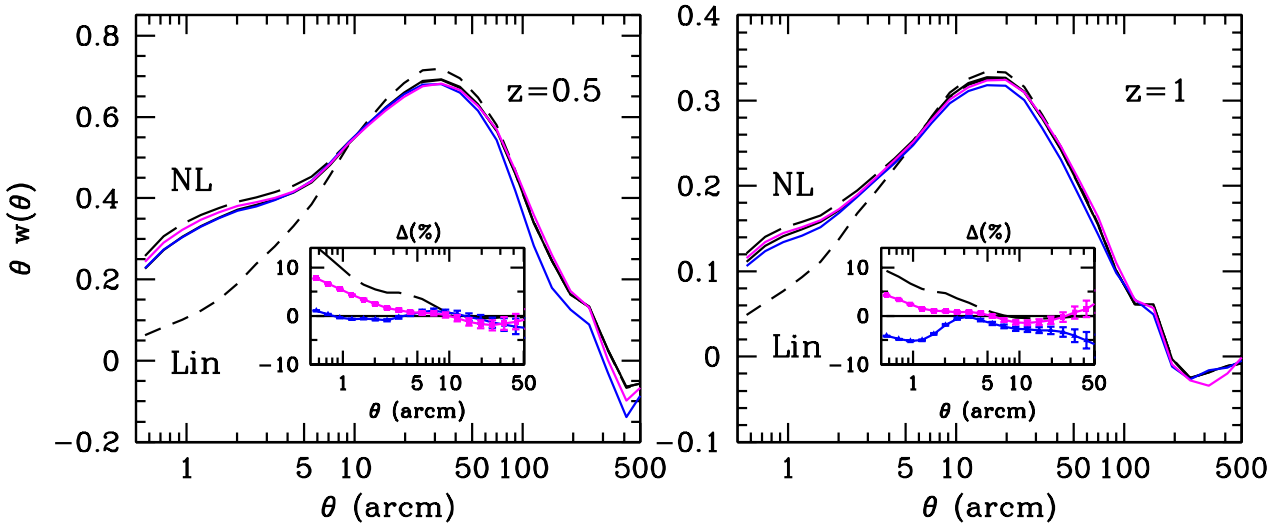


Figure 8. Same as Fig. 7 but for the angular 2-point correlation function. In order to better compare to theory predictions we use lines (instead of symbols) to display MICE-GC measurements. The inset panels display the ratio of measurements (and revised halofit) to the Smith et al. (2003) halofit prediction. We zoom into smaller angular scales to highlight mass resolution effects.

fields on the sphere, C_ℓ , as follows,

$$\langle X_{\ell m}^* Y_{\ell' m'} \rangle = \delta_{\ell\ell'} \delta_{mm'} C_\ell^{XY}, \quad (2)$$

where X and Y are two arbitrary 2D fluctuating fields.

Figure 7 shows the angular power spectrum for all-sky projected dark-matter overdensity in narrow redshift slices, for the MICE-GC, compared to a previous lower-mass resolution run, the MICE-IR. Particle shot-noise, shown as solid lines at the right of the upper panels, has been subtracted from the measured power spectra and displayed theoretical error bars correspond to an (ideal) all-sky survey. Throughout this paper, we shall use Gaussian theoretical error bars for the different observables of 2D clustering, unless otherwise stated, following Cabre et al. (2007); Crocce et al. (2011). We shall stress that this is an optimistic error estimate on small scales, since a significant deviation from the Gaussian approximation is expected to arise as a result of non-linear gravitational growth (Scoccimarro et al. 1999).

As shown in the lower panels of Fig. 7, using a particle mass 8 times lower, produces a drop in the measured power at the 5% level for multipoles $\ell \sim 10^3$, which corresponds to wavenumbers $k \sim 0.75$ at $z = 0.5$ and $k \sim 0.5$ for $z = 1$ in the flat-sky (or Limber) limit. The impact of such mass-resolution effect is even larger for higher redshift. This is consistent with the effect seen in the 3D power spectrum (see Figure 5). The fact that the magnitude of mass-resolution effects (and its dependence with redshift) at these quasi-linear scales are consistent in 3D comoving versus 2D lightcone outputs implies that possible lightcone artifacts (e.g. interpolation issues between lightcone time-steps) do not affect our results. For even smaller scales ($10^3 < \ell < 10^4$) the difference rises up to 10% – 20%, although here the amplitude of the effect and its scale-dependence start to be sensitive to the details of the shot-noise correction. Besides, at these highly non-linear scales, we cannot exclude possible lightcone interpolation artifacts, but again these would be difficult to separate from other sources of error such as inaccurate shot-noise correction. Comparing to state-of-the-art numerical fits, the MICE-GC measurements in the range $10^3 < \ell < 10^4$ show an 5 – 10% excess relative to Halofit (Smith et al. 2003), and a 5 – 10% deficit with respect to the revised Halofit by Takahashi et al. (2012), based on small-box high-resolution Nbody simulations. This trend of increasing power excess as one uses higher-resolution simulations indicates that what we observe on these scales is also consistent with the impact of mass-resolution on the clustering.

Any inconsistency in the parameters used for the simulations compared above could question the robustness of our conclusions. In particular, MICE-GC which uses the exact transfer function (computed with CAMB) to generate the initial conditions, whereas MICE-IR employs the Eisenstein & Hu (EH) approximation to the exact transfer function. However, differences between the exact and EH power spectrum are typically within 2% for $k \lesssim 10$, which corresponds to

multipoles $\ell \lesssim 10^4$ for $z > 0.5$. Therefore the observed discrepancy in the angular power spectra cannot be attributed to this slight inconsistency in the initial conditions. Other effects on this ℓ range, such as transients from initial conditions (see Crocce et al. (2006)), are expected to have a negligible impact for the MICE-GC outputs on these scales, but a detailed discussion will be presented elsewhere.

In Figure 8 we show the equivalent of Figure 7 but for the angular 2-point correlation function (A2PCF), i.e., the Legendre Transform of the angular power spectrum,

$$w(\theta) = \sum_{\ell} \frac{2\ell + 1}{4\pi} C_{\ell} L_{\ell}(\cos\theta), \quad (3)$$

where L_{ℓ} are the Legendre polynomials of order ℓ . It is clearly observed that there is a transfer of power from large (linear) to small (non-linear) angular scales as a result of gravitational growth. Theory fits predict that the amplitude of this transfer of power, as well as the angular scale that separates linear and non-linear regime increases with decreasing redshift. In particular, this transition angle is expected to be at $\theta \simeq 10$ arcminutes for $z = 0.5$ and $\theta \simeq 5$ arc-minutes for $z = 1$, in good agreement with measurements from simulations. Note that these scales do not correspond to what is naively expected by using the relation between multipoles and angular scales in the sky, $\theta = 180^\circ/\ell$. In practice this is because there are cancellations of nonlinear effects in configuration space which extend the apparent validity of linear theory to smaller scales (Crocce & Scoccimarro 2008). Because the transformation to Fourier (or multipole) space mixes the scales in the A2PCF for which the cancellation occurs nonlinear effects appear at smaller ℓ values in C_{ℓ} . This makes the 1-to-1 relation above mentioned not to strictly hold.

In a similar manner mass resolution effects are found to be smaller by roughly a factor of 2 in the A2PCF with respect to the angular power spectra for the same redshift bins and corresponding angular scales if the 1-to-1 relation would hold (see Figures 7 & 8). We find a 5 – 10% and 10 – 20% effect for $w(\theta)$ and the C_{ℓ} 's respectively for broad redshifts bins in the range $z = 0.5 - 1$. On the other hand on linear scales, $\theta \gtrsim 30 - 60$ arcmin depending on redshift, MICE-IR results clearly deviate from those of MICE-GC (and theory predictions). This can be due to a good extent to the different transfer function used to set up the initial conditions in both simulations. As shown in Figure 5, there are $\gtrsim 4\%$ differences between the initial power spectra of these two MICE simulations at $k \lesssim 0.1 h \text{ Mpc}^{-1}$, what corresponds to angular scales of $\theta = 180^\circ/(kr(z)) \simeq 80$ and 45 arcmin, in the Limber or small-angle limit, for $z = 0.5$ and $z = 1$, respectively.

4.2 Angular Clustering in Redshift Space

In this section we discuss the impact of peculiar velocities (or redshift space distortions) in the angular power spec-

tra and correlation function of dark-matter over-densities. Redshift space distortions (RSD) do not change the angular position of a *single* galaxy, nor they change significantly its measured redshift in photometric surveys. However the coherent large-scale motions present in RSD can have a large impact on the net angular correlation in a *sample* of galaxies. In particular, when the boundaries of the galaxy sample are defined in redshift space (as it happens in a real survey) then large-scale motions move structures across the boundaries in a spatially coherent way. In particular, the so-called Kaiser effect (Kaiser 1987) produces a large enhancement of the resulting angular correlations (see e.g., Crocce et al. (2010); Nock et al. (2010)). Although the use of photometric redshifts tends to counteract the correlations enhancement due to RSD by smoothing the 2PCF, the impact of RSD is still measurable in photometric surveys. This impact is seen as a net enhancement of the correlations measured in photometric surveys with respect to that expected in real space, and depends on the particular choice of redshift bin-width, being larger for narrower bins (as shown in our Figs 9 & 10 below, or Fig.5 in Crocce et al. 2011).

Below we shall model RSD for both broad and narrow redshift bin widths. The former is important for research that aims at measuring the growth of structure through RSD in photometric surveys (Padmanabhan et al. 2007; Ross et al. 2011; Crocce et al. 2011; Asorey et al. 2013). The later scenario is very relevant for recent studies that combine RSD in spectroscopic surveys with weak gravitational lensing, to break degeneracies between bias and dark energy parameters (Gaztañaga et al. 2012; Kirk et al. 2013; de Putter et al. 2013; Kirk et al. 2013; Font-Ribera et al. 2013).

Let us start by comparing the angular power spectrum in lightcone dark-matter outputs in real and redshift space from large linear scales (i.e low multipoles) to small and non-linear scales (high-multipoles). In Figure 9, we show results for dark-matter sources in the light-cone at mean redshifts, $z = 0.5$ and 1 . In order to see the impact of projection effects, we display results for two cases, broad $\Delta z = 0.1$ (left panels) and narrow $\Delta z = 0.01$ (right panels) redshift bins. Theory predictions, computed with `CAMB sources`, are given in the linear and non-linear regime for the growth of structure (Halofit, solid lines). However, theory RSD effects are only computed in the linear regime, the so-called Kaiser effect.

In Fig. 9, both theory and simulation results are normalized to the non-linear Halofit (Smith et al. 2003) predictions in real-space (labeled “halofit, real-space” in plots). Simulations show that RSD effects enhance the large-scale (low- ℓ) clustering relative to real-space, by a factor of $\simeq 3$ (although it depends slightly on redshift), in agreement with the Kaiser effect (e.g. Padmanabhan et al. (2007)). This is also clearly seen in configuration space, see Fig. 10, where simulations accurately recover the Kaiser “boost” for an-

gular scales $\theta \gtrsim 50 - 100$ arcmin. In particular, the Kaiser boost also enhances the BAO feature on few degree angular scales, an effect that has been studied in depth in the context of upcoming photometric surveys (Crocce et al. 2010; Nock et al. 2010).

On the other hand, non-linear RSD caused by random motions in virialized dark-matter halos tend to suppress power on small-scales relative to 3D clustering in real-space. This is only seen in 2D clustering for sufficiently narrow redshift bins, this is, when projection effects do not cancel out completely random peculiar motions along the line of sight. We find a $\simeq 2\%$ power suppression on non-linear growth scales ($\ell \gtrsim \ell_{NL-growth} \simeq 300$) for $\Delta z = 0.1$, and we observe this relative suppression grows roughly proportional to the inverse of the z-binwidth Δz ,

$$\left| \frac{C_\ell(\text{redshift} - \text{space}) - C_\ell(\text{real} - \text{space})}{C_\ell(\text{real} - \text{space})} \right| \simeq \frac{2 \times 10^{-3}}{\Delta z} \quad (4)$$

so that redshift-space angular clustering is $\simeq 20\%$ lower than in real-space for the narrow bin, $\Delta z = 0.01$, in the non-linear regime. It is interesting to see that non-linearities in RSD, as seen in the simulation (see red symbols, as compared to linear RSD theory given by the red lines), appear at much lower multipoles, $\ell_{NL-RSD} \gtrsim 30 - 50$, than those where gravitational growth enters the non-linear regime, $\ell_{NL-growth} \gtrsim 500 - 10^3$, where the lower (higher). estimates correspond to $z = 0.5$ and 1 respectively. In particular, we find that $\ell_{NL-RSD} \simeq \ell_{NL-growth}/10$, for the bin widths studied. This is a consequence of the fact that velocities have more power on weakly nonlinear scales than densities, in addition to pairwise velocity dispersion effects that enter in RSD (the so-called Finger-of-God effect). For an order of magnitude estimate these effects enter through a damping factor $\propto \exp(-f^2 k_z^2 \sigma_v^2)$ where σ_v is the 1D linear velocity dispersion and f the growth rate¹³. If we set this to introduce a 10% damping along the line-of-sight then $f^2 \sigma_v^2 \sim 0.1/k^2 \sim 0.1 r^2(z)/\ell^2$. At $z = 0.5$ where $\sigma_v \sim 5 h^{-1}$ Mpc and $f \sim 0.7$ this translates into $\ell_{NL-RSD} \sim 100 - 150$. Moreover we find a similar estimated value of ℓ_{NL-RSD} for $z = 1$. This is fully compatible with our findings for narrow band binnings in Fig 9 (while broad-band binning erase to large degree this line-of-sight effects).

Alternatively, non-linear RSD effects in the 2PCF $w(\theta)$ are significant on scales $\theta_{NL-RSD} \lesssim 100$ arcmin. In analogy to what we found in harmonic space, this angular scale is roughly an order of magnitude larger than the transition scale to non-linear gravitational growth, $\theta_{NL-growth} \simeq \theta_{NL-RSD}/10 \simeq 10$ arcmin, as shown in Figure 10. The amplitude of non-linear RSD effects, estimated as the difference between the linear RSD theory prediction (red solid line) and the simulation measurement (red symbols) on $\theta < \theta_{NL-RSD}$, is $\simeq 2\%$ on non-linear scales for the broad z-bin,

¹³ This is discussed in detail in Sec. 6.2 of Paper II

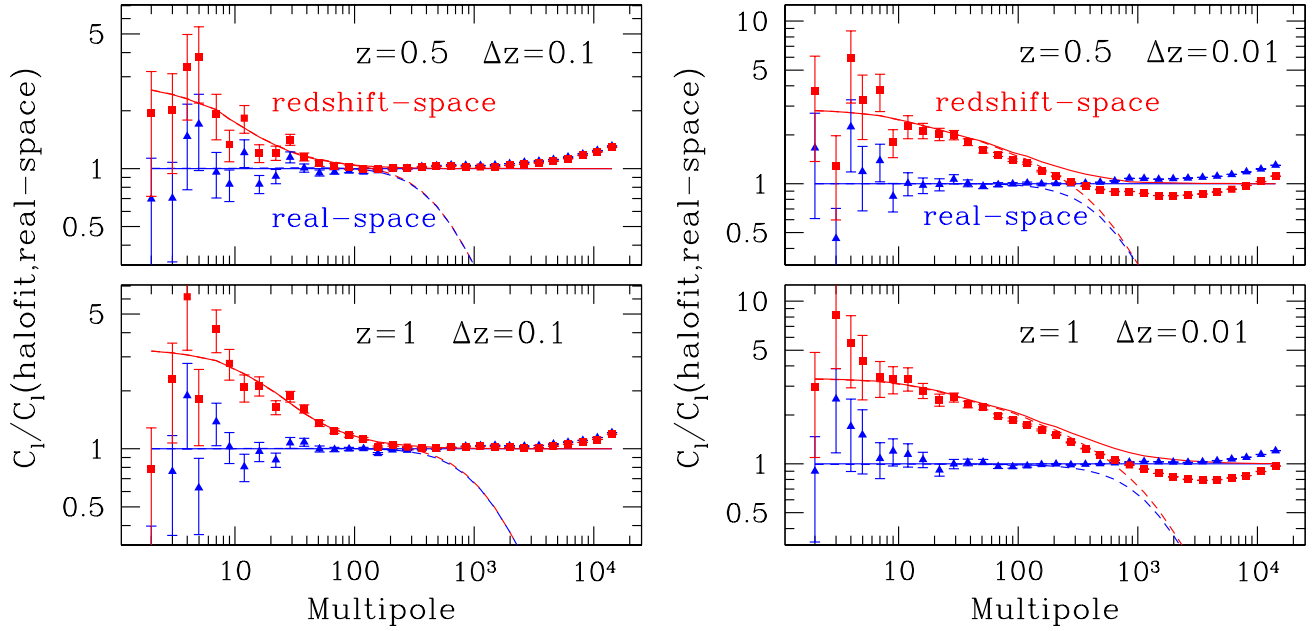


Figure 9. Comparison between angular clustering in real and redshift space. Left panels show results for $z = 0.5, 1$ for two broad redshift bins, $\Delta z = 0.1$. Theory predictions are given in the linear (dashed) and non-linear regime of gravitational clustering (Halofit, solid lines). Theory RSD effects are only modeled in the linear regime (i.e., Kaiser effect), following the CAMB implementation. Symbols display measurements in the MICE-GC simulation. Both theory and simulation results are normalized to non-linear theory predictions in real-space (labeled “halofit, real-space” in the Figures). Simulations show that RSD effects enhance the large-scale (low- ℓ) clustering relative to real-space, by a factor of $\simeq 3$, in agreement with linear predictions (red lines). Non-linear RSD tend to suppress power on small-scales. This is only significant in 2D clustering for sufficiently narrow redshift bins, e.g. $\Delta z = 0.01$ (see right panels).

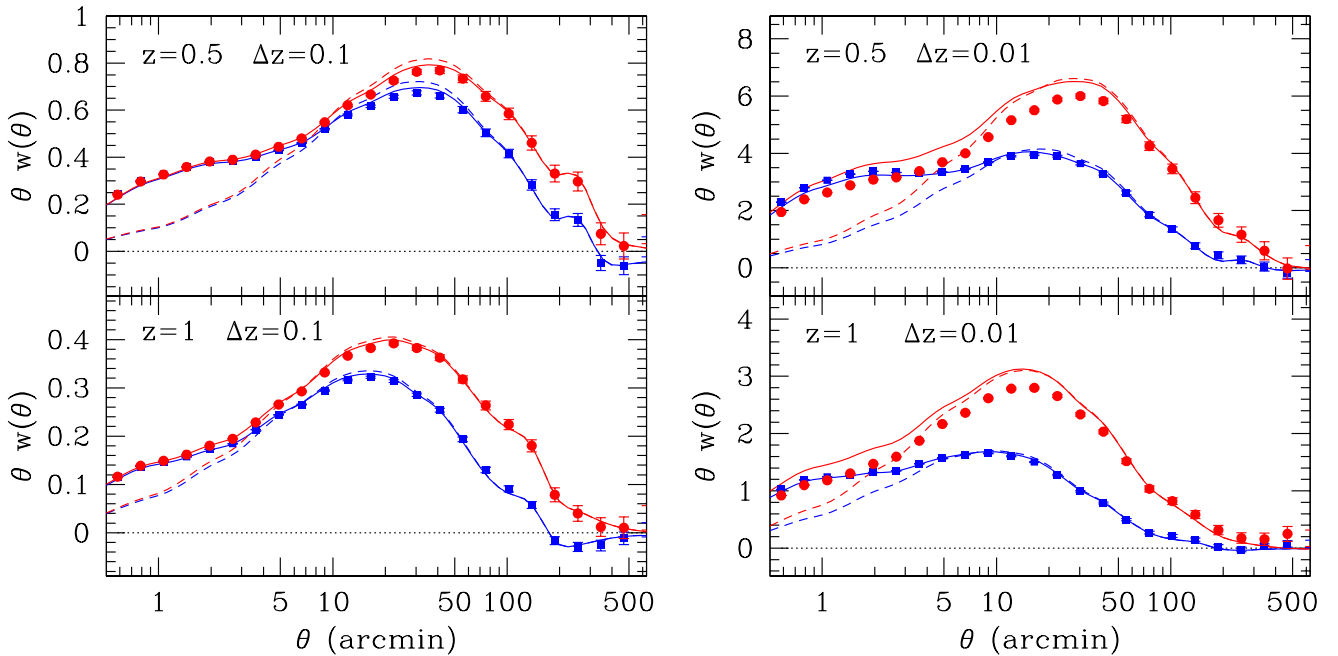


Figure 10. Same as Figure 9 but for the angular 2PCF. The theory predicted Kaiser effect is recovered in the simulation for $\theta \gtrsim 50 - 100$ arcmin, where coherent motions of dark-matter particles tend to enhance clustering by a factor, $\simeq 3$. For narrow z -bins (right panels) non-linear RSD appear at $\theta \lesssim 100$ arcmin, where the simulation (red symbols) deviates from linear RSD theory (red solid lines).

$\Delta z = 0.1$, and up to $\simeq 5 - 15\%$ for scales $\theta = 60 - 1$ arcmin respectively, for the narrow z -bin. These amplitudes are in agreement with the results found for the angular power spectra at the highest multipoles (i.e., non-linear scales), Fig.9.

5 HIGHER-ORDER CLUSTERING: 3-POINT CORRELATION FUNCTION

5.1 Mass-resolution effects

The 2 and 3-point correlation functions are defined, respectively, as

$$\xi(r_{12}) = \langle \delta(r_1)\delta(r_2) \rangle \quad (5)$$

$$\zeta(r_{12}, r_{23}, r_{13}) = \langle \delta(r_1)\delta(r_2)\delta(r_3) \rangle \quad (6)$$

where $\delta(r)$ is the local density contrast at position r smoothed over a given characteristic R scale, and the 2-point function is the Fourier transform of the power spectrum shown in §3.1. The reduced 3-point function Q_3 (Groth & Peebles 1977) is defined as:

$$Q_3 = \frac{\zeta(r_{12}, r_{23}, r_{13})}{\zeta_H(r_{12}, r_{23}, r_{13})} \quad (7)$$

$$\zeta_H \equiv \xi(r_{12})\xi(r_{23}) + \xi(r_{12})\xi(r_{13}) + \xi(r_{23})\xi(r_{13}),$$

where we have introduced a definition for the "hierarchical" 3-point function ζ_H . Based on early galaxy measurements of ζ , the Q_3 parameter was thought to be roughly constant as a function of triangle shape and scale, a result that is usually referred to as the hierarchical scaling. It was later shown (Peebles 1980; Fry 1984) that one expects deviations from this scaling in the weakly non-linear regime due to gravitational clustering starting from Gaussian initial conditions, which enhances the filamentary structure and produce anisotropic values of Q_3 and ζ as we change the shape and size of the triangles.

To illustrate the dependence of Q_3 on the triangle shape we will fix two of the triangle sides (r_{12}, r_{13}) and display results as function of the third side r_{23} . Figure 11 shows a comparison of Q_3 as measured from the MICE simulations of different particle resolutions. We also show the predictions from tree-level perturbation theory (PT, from Barriga & Gaztañaga (2002)) using different transfer functions in the initial conditions (i.e., CAMB and EH) and the no-wiggle model of EH, i.e. without the BAO peak. We have found very little change of Q_3 with redshift within the errors, so these results are very similar for $0 < z < 1$ (see also Fig. 14 below).

We can see a small, but systematic and significant, dependence on the simulation mass particle resolution that are comparable in order of magnitude to the deviations between simulations and PT and also the differences between different transfer functions. The biggest discrepancy is with the model without a BAO, indicating that the BAO can be clearly detected in Q_3 in our simulations (see Gaztañaga

et al. (2009) and references therein for measurements of this effect). These results can only be achieved with the largest volumes (and therefore at higher redshifts in the lightcone).

The discrepancies at the 2-point function level, i.e. in ζ_H , are comparable to what we show in previous sections and can be understood using the halo model. The higher the resolution the lower mass halos that we can resolve. This results in higher power on the smallest scales, corresponding to the smallest mass halos that are resolved. For the 3-point function, the effect comes from the mode coupling which makes the clustering anisotropic. This results in a characteristic anisotropic shape of Q_3 or ζ as a function of the triangle shape (which is given by a U-Shape as a function of r_{23} in Fig. 11). Non-linear dynamics tend to reduce this shape dependence and makes clustering more isotropic, specially on the smaller scales (e.g. see Bernardeau et al. (2002)). This could explain why a better resolution of non-linear effects (which comes with higher particle resolution) results in slightly more isotropic clustering, which in our case means slightly lower amplitudes of Q_3 and ζ for elongated triangles, as shown in Fig. 11.

Figure 12 illustrates these arguments in more detail. Here we show the differences between measurements and leading order perturbation theory (PT) for triangles that are a factor of 2 smaller. This result in smaller errors, that are useful to appreciate some trends. We can see how MICE-GC, the higher resolution simulation (squares), does not change much with redshift (compare right to left panels) and shows deviations from PT that are small but significant. These are caused by higher order (loop) corrections in PT. As in the leading order contribution to Q_3 , these corrections also originate in the non-linear mode coupling between scales. To guide the eye, we match these differences with an ad-hoc amplitude:

$$Q_3 - Q_3^{PT} \simeq AQ(\beta) + B \quad (8)$$

where $Q(\beta)$ corresponds to the quadrupole in the mode coupling term from Euler's equation (Eq. (38) in Bernardeau et al. (2002)), i.e. gradients of the velocity divergence in the direction of the flow. This is shown as dashed lines in Figure 12. In contrast, we can see in Figure 12 that the lower resolution simulations show more evolution. At $z = 0$ (left panel) all results tend to agree (except the co-linear configurations for the lower resolution, which are still converging). At $z = 1$, the intermediate resolution (IR-MICE) show a significant difference in configuration, with a tendency of being less sensitive to the configuration (shape of triangle) than the higher resolution simulation. At higher redshifts, the resolution effects become more important as non-linearities affect larger scales than at lower redshifts. For the 2-point function this results in lower clustering (e.g. see discussion around Fig.5.). For Q_3 this translates into smaller mode coupling and less configuration dependence. For precision measurements and interpretation (of galaxy bias models, see paper II) these differences are significant

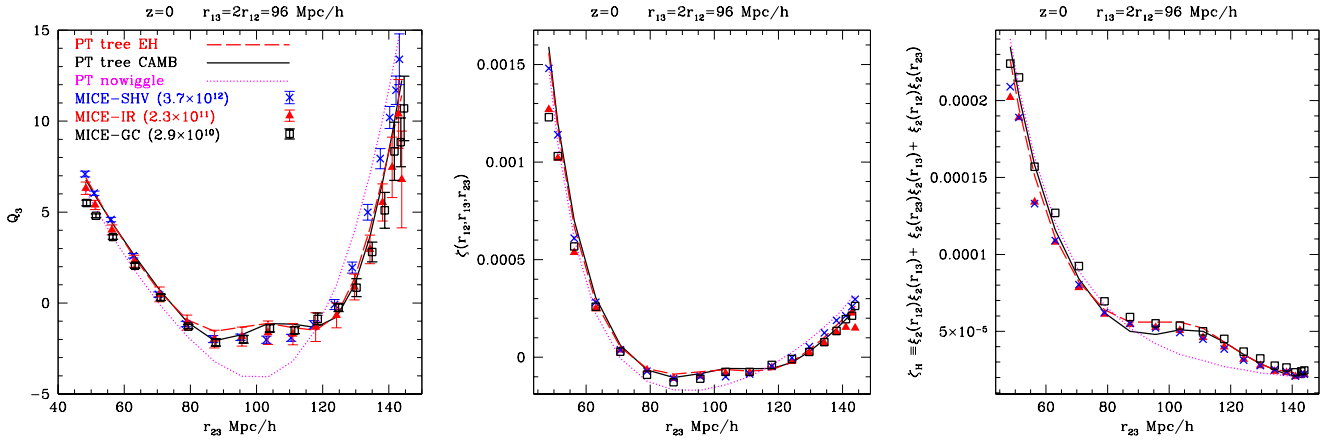


Figure 11. Reduced 3-point $Q_3(r_{12}, r_{13}, r_{23})$ (left panel), which is the ratio, see Eq. 7, of the 3-point $\zeta(r_{12}, r_{13}, r_{23})$ (middle panel) to the hierarchical 2-point product $\zeta_H \equiv \xi(r_{12})\xi(r_{23}) + \xi(r_{12})\xi(r_{13}) + \xi(r_{23})\xi(r_{13})$ (right). This is for $z=0$ and $r_{13} = 2r_{12} = 96$ Mpc/h, as a function of r_{23} . MICE simulations of different resolutions (as labeled in the top panel) are compared to PT results with different IC (transfer functions), including the case without BAO (no-wiggles). The BAO peak can be clearly seen as a bump around $110 h^{-1}$ Mpc in all panels. A lack of resolution reduces the power in the 2-point ζ_H , but increases slightly the anisotropy in the 3-point ζ . Both effects makes Q_3 significantly more anisotropic as we reduce the mass resolution in the MICE simulations.

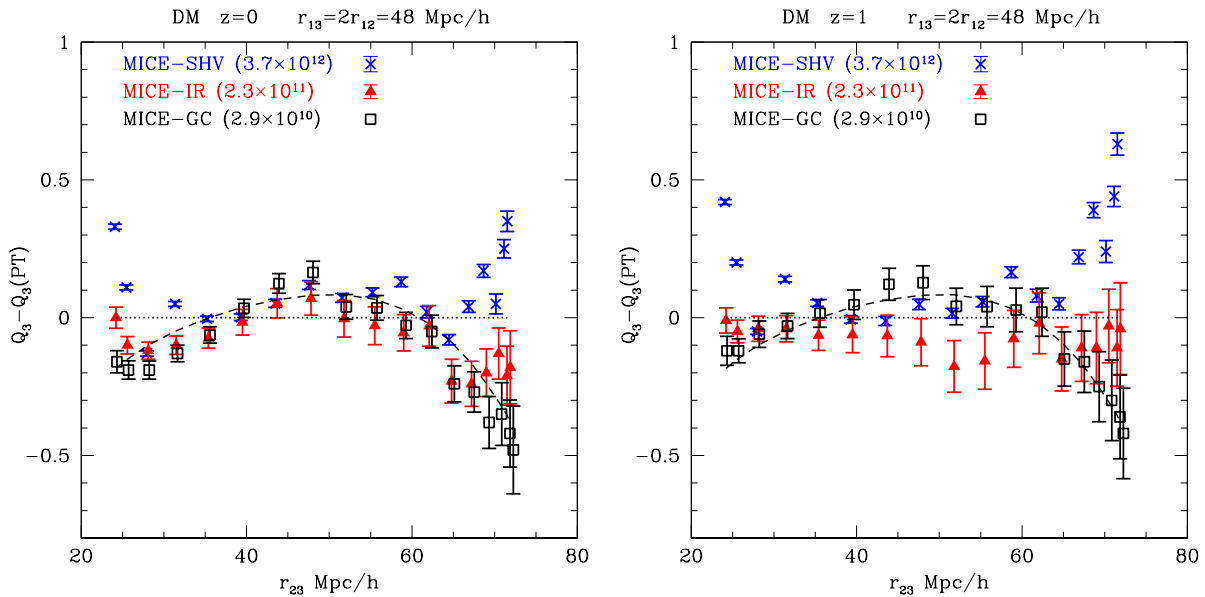


Figure 12. The difference between leading order perturbation theory (PT) results and measurements in simulations with different resolutions. In each case we use the corresponding transfer function to estimate the PT results. This is for triangles with $r_{13} = 2r_{12} = 48$ Mpc/h and shown as a function of the remaining leg r_{23} . As the simulation evolves the different resolution converge to each other (left, $z=0$), but note how at earlier times (right, $z=1$), the lower resolutions produce quite different results. The dashed lines includes an additional tidal component that matches the high resolution simulation (to guide the eye).

and affect resolutions ($\sim 10^{11}$) that are often used to study the shape dependence in Q_3 and its biasing (e.g. see Manera & Gaztañaga (2011) and references therein).

Figure 13 shows these differences more clearly at $z = 0$ and smaller scales ($r_{13} = 2r_{12} = 24 h^{-1}$ Mpc) as a ratio of Q_3 in the lower resolution simulations (MICE-IR and MICE-SHV) with respect to the value of Q_3 in the high-

est resolution (MICE-GC, $2.9 \times 10^{10} h^{-1} M_{\odot}$ particle mass). Error-bars are given by the shaded region. Overall deviations are around 5% and as large as 10 – 15% for the lowest resolution run (MICE-SHV, $3.7 \times 10^{12} h^{-1} M_{\odot}$ particle mass). For a particle mass of $2.3 \times 10^{11} h^{-1} M_{\odot}$, as in MICE-IR, deviations are around 2% and always smaller than 5%. These deviations are significant, given the error-bars, and

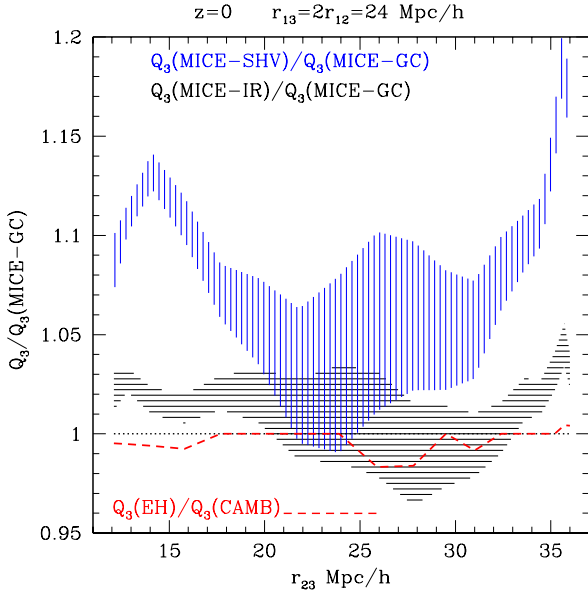


Figure 13. This is similar to Fig.11 but for smaller scales $r_{13} = 2r_{12} = 24$ Mpc/h. Here we show the ratio of the low resolution results with respect to the one with highest resolution (MICE-GC). Deviations from unity are significant given the errors (shaded regions) and do not seem to arise from small differences in the transfer functions used (dashed lines).

can not be explained by the differences in the transfer function shown in Fig. 5 which, at these scales, are smaller than 1% is Q_3 (i.e., dashed line).

The observed trend of increasing mass-resolution effects as one samples smaller (more non-linear) scales seems consistent with previous analyses of the 3-point function on even smaller scales, i.e., ~ 1 Mpc/h (Fosalba et al. 2005), where measurements on comparable resolution simulations exhibit more configuration dependence than the halo model predictions (see bottom panels of their Fig.10).

5.2 Realization effects

In some particular triangular configurations, when we have very large scales $r \simeq 80 - 100 h^{-1}$ Mpc but small errors, we can detect some systematic differences that seem to be caused by the power spectrum realization. When using a single simulation, the simulated spectrum is typically slightly different to input transfer at the largest scales because of sampling variance. This is illustrated in Fig. 14 which compares configurations with $r_{12} = r_{13} = 48 h^{-1}$ Mpc in MICE simulations that uses EH and **CAMB** transfer functions. On both the largest scales ($r_{23} \simeq 90 - 100 h^{-1}$ Mpc) and intermediate scales ($r_{23} \simeq 40 - 70 h^{-1}$ Mpc) the values of Q_3 are significantly different in the two simulations. The differences at intermediate scales can be understood because of the difference in the initial transfer function of the simulations. When we compare the results to the corresponding

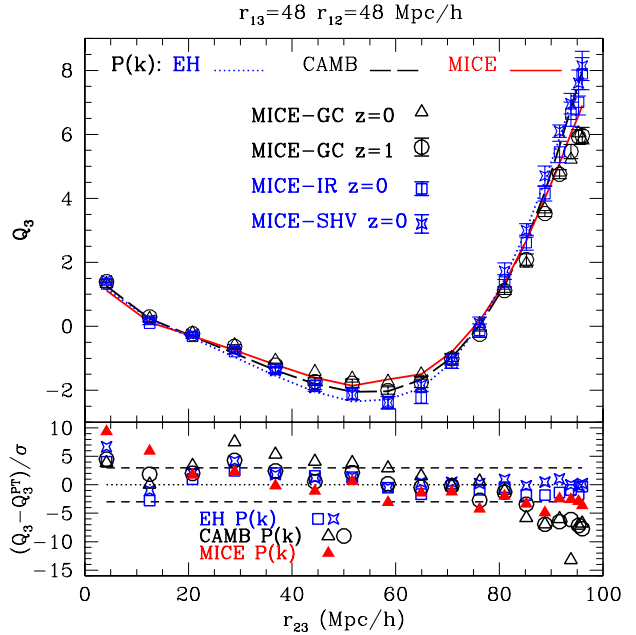


Figure 14. Comparison of $Q_3(r_{23})$ measurements (symbols) for $r_{13} = r_{12} = 48 h^{-1}$ Mpc in different MICE simulations, with predictions (lines) based on the initial transfer function $P(k)$ used in each simulation (EH for IR and SHV, and **CAMB** for GC). Measurements in MICE-IR (squares) and MICE-SHV (stars) agree well with predictions from EH transfer function. MICE-GC measurements (triangles and circles) are significantly lower than the **CAMB** predictions at the largest scales, but give comparable results at $z=0$ and $z=1$. The bottom panel shows the significance of the differences with respect to the corresponding prediction. The MICE-GC result compared to **CAMB** (open circles and triangles) show more than $5\text{-}\sigma$ deviations at scales $r_{23} > 90 h^{-1}$ Mpc. This discrepancy reduces to $3\text{-}\sigma$ when we use the prediction estimated using the measured MICE-GC $P(k)$ (closed triangles).

PT predictions (in the bottom panel) we find no significant deviations (within $3\text{-}\sigma$ errors) between measurements and (tree-level) PT results on this intermediate scales, also indicating that particle resolution does not seem so important for these configurations, given the errors. Note that the errors in MICE-GC and MICE-IR are from Jack-knife (JK) resampling, while the error in MICE-SHV are obtained by dividing the very big box into 27 subsamples.

On the largest scales, the differences between the EH and **CAMB** transfer functions are small (i.e., compare dotted line to dashed line, which lie on top of each other for $r_{23} > 90 h^{-1}$ Mpc), but the MICE-GC simulation (circles and triangles) seem significantly lower than the MICE-IR or MICE-SHV results. We find very similar results at other redshifts. The differences are not caused by the binning in the scales defining the sides of the triangles (r_{12}, r_{13}, r_{23}) and the effect does not seem to be caused by resolution (given the agreement within errors with the corresponding predictions at lower scales and the agreement on all scales between MICE-IR and MICE-SHV). These differences seem

to originate in sampling variance in the realization of the initial transfer function of the MICE-GC simulation on the smallest k -modes.¹⁴ This is hinted when comparing the open and closed (red) triangles in the bottom panel. Here the open triangles compare MICE-GC ($z=0$) measurements to the **CAMB** prediction (which is the input to the MICE-GC simulation), while closed triangles compare the same measurements to the predictions based on the actual measured MICE-GC power spectrum. This is different from the **CAMB** predictions because of sampling variance in the MICE-GC realization of the **CAMB** transfer function. While deviations with the **CAMB** $P(k)$ predictions are quite significant (between 5 and 10 σ), deviations with the MICE-GC $P(k)$ predictions are lower (within 3 σ). The values at $z=1$ (squares) show a similar trend, indicating that this is not just an evolution effect. This figure also illustrates how Q_3 does not evolve much with redshift (compare circles, $z=1$, and open triangles, $z=0$) and that PT predictions are more accurate for intermediate scales than for small or large scales: i.e., it fails more for triangles that are collapsed (see also Bernardeau et al. (2002)). As discussed above, the lower resolution simulations (squares and stars) seem to agree better with PT results because of the artificial suppression of non-linearities (i.e., due to poor mass resolution).

Once we use the right shape of the power spectrum, the measurements seem to match predictions within $3\text{-}\sigma$ (dashed lines in bottom panel), although the agreement is even better for triangles that are less collapsed. In general, we do not expect tree-level PT to match the simulations perfectly and some deviations are expected due to higher-order (loop) corrections (see Bernardeau et al. (2002)).

6 CONCLUSIONS

We have presented one of the largest Nbody runs completed to date: the MICE Grand Challenge Lightcone simulation (MICE-GC), containing about 70 billion particles in a 3 Gpc/h periodic box. This combination of large volume and fine mass resolution allows to resolve the growth of structure from the largest (linear) cosmological scales down to very small (tens of kpc's) scales, well within the non-linear regime. Therefore, the MICE-GC presents multiple potential applications to study the clustering and lensing properties of dark-matter and galaxies that can be confronted with observations from upcoming galaxy surveys.

Furthermore we have populated halos with galaxies using a hybrid HOD and HAM scheme and studied their clustering and lensing properties. Clustering results from the halo and galaxy catalogs are presented in an accompanying paper (Paper II, Crocce et al. (2013)), whereas the all-sky

lensing maps and galaxy lensing properties modeled with this new mock are discussed in Paper III (Fosalba et al. 2015). Further details about the galaxy assignment method implemented to build the MICE-GC mock galaxy catalog will be presented in forthcoming papers (Carretero et al. 2014, Castander et al. 2014).

We make a first public data release of the MICE-GC galaxy mock, MICECAT 1.0, through a dedicated web-portal for simulations, hosted by the Port d'Informacio Cientifica (PIC): <http://cosmohub.pic.es>, where detailed information on the data provided can be found.

In this first paper of the series (Paper I), we have discussed a basic validation and the applications for the dark-matter comoving and lightcone outputs, using 2D and 3D statistics. Throughout the paper we have investigated how mass-resolution effects impact dark-matter clustering in the non-linear regime. In other words, we have discussed how much our N-body measurements on small scales might be limited by the particle mass used. Although a proper systematic study based on an ensemble of simulations will be presented elsewhere, we have obtained a series of results and conclusions from the MICE-GC run alone that we summarize below.

The main findings of this paper are as follows:

- Using MICE-GC we can measure the BAO pattern in the 3D dark-matter power spectrum with high precision. We find very good agreement with Renormalized Perturbation Theory (RPT) predictions at two-loops and $k \lesssim 0.2\text{--}0.3 h \text{ Mpc}^{-1}$, see Fig. 3. There is also a good match comparing to state-of-the-art numerical fits, although we find a slight excess broad-band power ($\lesssim 2\%$) with respect to the extended Coyote emulator (Heitmann et al. 2013) and the revised Halofit (Takahashi et al. 2012) at $z > 0$. We note that these differences appear larger than our statistical error bars on those scales (see Figs. 3 and 4).
- Detailed comparison across redshift evolution and non-linear scales between the power spectrum measured in MICE-GC and recent numerical fits shows that they agree well, but the latter seem to slightly over-predict the power on BAO scales, specially at $z > 0$ (see Fig.4). This is more clearly seen beyond BAO scales ($k > 0.3 h^{-1} \text{ Mpc}$) for the recently revised Halofit fitting formula where the effect reaches 5% – 8% depending on redshift.
- By comparing the 3D power spectrum of MICE-GC to an order of magnitude lower resolution run with the same cosmology, the MICE-IR, we conclude that the change in clustering power produced by mass resolution effects increase with decreasing scale and grow with redshift. Resolution effects are within 2% for $k < 0.2 h \text{ Mpc}^{-1}$ for $z < 1$, but can be as large as 5% for $k \simeq 1 h \text{ Mpc}^{-1}$ and $z = 1$, as shown in Fig. 5.
- We have also produced lightcone outputs of the MICE-GC run, following the approach presented in Fosalba et al. (2008). As shown in Fig. 7, the analysis of angular clus-

¹⁴ This variance is not captured by our Q_3 JK error-bars as it is based on sampling the spatial variations within the one single realization of the **CAMB** power spectrum.

tering of the projected dark-matter in the lightcone yields consistent qualitative results: the MICE-GC measures a 5% excess power for multipoles $\ell \sim 10^3$ with respect to the lower-resolution run. But this grows to 20 – 30% excess for multipoles $\ell > 10^3$, which correspond to $k \gtrsim 0.75$ at $z = 0.5$, and $k \gtrsim 0.5$ for $z = 1$ in the Limber or small-angle limit. This confirms that the observed power excess is largely due to mass resolution effects. Moreover the impact of such resolution effect is even larger for higher redshift, as shown in Fig. 7. This is consistent with what we found from the 3D power spectrum analysis. Similar trends are found in the angular 2-point function, as shown in Fig. 8.

- Comparison of angular power spectra with recent numerical fits shows that the MICE-GC measurements show an 5 – 10% excess relative to Halofit (Smith et al. 2003) in the range $10^3 < \ell < 10^4$, and a 5 – 10% deficit with respect to the revised Halofit by Takahashi et al. (2012).

- The modeling of the RSD effects in angular clustering, investigated in §4.2, concludes that MICE-GC recovers the Kaiser effect on large scales, i.e., a boost of power of order $\simeq 3$ relative to the real-space counterpart. On the other hand, non-linear RSD caused by random motions in virialized dark-matter halos tend to suppress power on small-scales relative to 3D clustering in real-space. This is only seen in 2D clustering for sufficiently narrow redshift bins, and the amplitude of the effect roughly scales with the inverse of the redshift binwidth (see Eq. 4). In particular, nonlinearities in RSD, as seen in the simulation (see Fig. 9) appear at much lower multipoles than those where gravitational growth enters the non-linear regime. We find that $\ell_{NL-RSD} \simeq \ell_{NL-growth}/10$, and similar results hold for the angular 2PCF, i.e., $\theta_{NL-growth} \simeq \theta_{NL-RSD}/10 \simeq 10$ arcmin.

- For the 3-point function, we find consistent results with those of the 2-point statistics. Higher mass resolution runs resolve better the small-scale power which tends to flatten out the reduced 3-point function, Q_3 with respect to PT (tree-level) expectation. This effect seems to get worse at higher redshifts, as shown in Fig. 12. We show how the BAO signal can be detected in Q_3 , as indicated by measurements by Gaztañaga et al. (2009). On BAO scales errors are quite large and resolution effects are not very significant. On small scales ($12 - 24 h^{-1}$ Mpc), Fig.13 shows how the lower resolution simulations, tend to estimate a more anisotropic 3-point function than the higher resolution ones, at the 5% level for MICE-IR and up to 15% for the MICE-SHV run (which has about 100 times larger particle mass than MICE-GC). On intermediate scales, the mass resolution produces differences that are systematic and significant. We have learned here that Q_3 is quite sensitive to the actual shape of the power spectrum but this can be degenerate with resolution effects for larger volumes, such as the ones in MICE simulations.

In summary this new large-volume simulation is shown to describe accurately dark-matter clustering statistics in

a wide dynamic range. From the linear to the highly non-linear regime of gravitational clustering, thanks to its adequate combination of large-volume and good mass resolution. The resulting galaxy mock MICECAT v1.0, described in the accompanying Papers II and III of this series, is made publicly available with the hope that it will be used as a powerful tool to develop and exploit the high quality data that is expected from the new generation of astronomical surveys.

ACKNOWLEDGMENTS

We would like to thank Volker Springel for useful discussions regarding Gadget2, Antony Lewis and Ruth Pearson for support with the CAMB `sources` code, Eric Hivon for help with Healpix and discussions about spherical harmonic analysis, and the Barcelona Supercomputing Center (BSC) support staff, specially David Vicente, for their continued support to develop this Grand Challenge simulation. Special thanks to Santi Serrano for his great help with the MICE website, the simulation visualizations, including Figure 1 in this paper, and for enlightening discussions that led to the development of the simulations web-portal. We are greatly indebted to Jorge Carretero, Christian Neissner, Davide Piscia, Santi Serrano and Pau Tellada for their development of the CosmoHub web-portal. We acknowledge support from the MareNostrum supercomputer (BSC-CNS, www.bsc.es), through grants AECT-2008-1-0009, 2008-2-0011 and 2008-3-0010, 2009-1-0009, 2009-2-0013, 2009-3-0013, and Port d'Informació Científica (www.pic.es) where the simulations were ran and stored, respectively, and the use of the Gadget-2 code to implement the N-body (www.mpa-garching.mpg.de/gadget). Funding for this project was partially provided the European Commission Marie Curie Initial Training Network CosmoComp (PITN-GA-2009 238356), the Spanish Ministerio de Ciencia e Innovación (MICINN), projects 200850I176, AYA-2009-13936, AYA-2012-39620, AYA-2012-39559, Consolidar-Ingenio CSD2007-00060 and research project SGR-1398 from Generalitat de Catalunya. MC acknowledges support from the Ramón y Cajal MICINN program.

REFERENCES

- Alimi J.-M., Bouillot V., Rasera Y., Reverdy V., Corasaniti P.-S., Balmes I., Requena S., Delaruelle X., Richet J.-N., 2012, ArXiv e-prints
 Angulo R. E., Baugh C. M., Frenk C. S., Lacey C. G., 2008, *MNRAS*, 383, 755
 Angulo R. E., Springel V., White S. D. M., Jenkins A., Baugh C. M., Frenk C. S., 2012, *MNRAS*, 426, 2046
 Asorey J., Crocce M., Gaztanaga E., 2013, ArXiv e-prints
 Barriga J., Gaztañaga E., 2002, *MNRAS*, 333, 443

- Bernardeau F., Colombi S., Gaztañaga E., Scoccimarro R., 2002, *Phys. Rep.*, 367, 1
- Cabre A., Fosalba P., Gaztanaga E., Manera M., 2007, ArXiv Astrophysics e-prints
- Crocce M., Cabré A., Gaztañaga E., 2011, *MNRAS*, 414, 329
- Crocce M., Castander F. J., Gaztanaga E., Fosalba P., Carretero J., 2013, ArXiv e-prints
- Crocce M., Fosalba P., Castander F. J., Gaztañaga E., 2010, *MNRAS*, 403, 1353
- Crocce M., Gaztañaga E., Cabré A., Carnero A., Sánchez E., 2011, *MNRAS*, 417, 2577
- Crocce M., Pueblas S., Scoccimarro R., 2006, *MNRAS*, 373, 369
- Crocce M., Scoccimarro R., 2008, *Phys. Rev. D*, 77, 023533
- de Putter R., Doré O., Takada M., 2013, ArXiv e-prints
- Dunkley J., Komatsu E., Nolte M. R., Spergel D. N., Larson D., Hinshaw G., Page L., Bennett C. L., Gold B., Jarosik N., Weiland J. L., Halpern M., Hill R. S., Kogut A., Limon M., Meyer S. S., Tucker G. S., Wollack E., Wright E. L., 2009, *Astrophys. J. Suppl.*, 180, 306
- Eisenstein D. J., Hu W., 1998, *Astrophys. J.*, 496, 605
- Feldman H. A., Kaiser N., Peacock J. A., 1994, *Astrophys. J.*, 426, 23
- Font-Ribera A., McDonald P., Mostek N., Reid B. A., Seo H.-J., Slosar A., 2013, ArXiv e-prints
- Fosalba P., Gaztañaga E., Castander F. J., Crocce M., 2015, *MNRAS*, 447, 1319
- Fosalba P., Gaztañaga E., Castander F. J., Manera M., 2008, *MNRAS*, 391, 435
- Fosalba P., Pan J., Szapudi I., 2005, *Astrophys. J.*, 632, 29
- Fry J. N., 1984, *Astrophys. J.*, 279, 499
- Gaztañaga E., Cabré A., Castander F., Crocce M., Fosalba P., 2009, *MNRAS*, 399, 801
- Gaztañaga E., Eriksen M., Crocce M., Castander F. J., Fosalba P., Marti P., Miquel R., Cabré A., 2012, *MNRAS*, 422, 2904
- Górski K. M., Hivon E., Banday A. J., Wandelt B. D., Hansen F. K., Reinecke M., Bartelmann M., 2005, *Astrophys. J.*, 622, 759
- Groth E. J., Peebles P. J. E., 1977, *Astrophys. J.*, 217, 385
- Heitmann K., Lawrence E., Kwan J., Habib S., Higdon D., 2013, ArXiv e-prints
- Kaiser N., 1987, *MNRAS*, 227, 1
- Kim J., Park C., Gott III J. R., Dubinski J., 2009, *Astrophys. J.*, 701, 1547
- Kim J., Park C., Rossi G., Lee S. M., Gott III J. R., 2011, *Journal of Korean Astronomical Society*, 44, 217
- Kirk D., Lahav O., Bridle S., Jouvel S., Abdalla F. B., Frieman J. A., 2013, ArXiv e-prints
- Klypin A., Prada F., Yepes G., Hess S., Gottlober S., 2013, ArXiv e-prints
- Manera M., Gaztañaga E., 2011, *MNRAS*, 415, 383
- Nock K., Percival W. J., Ross A. J., 2010, *MNRAS*, 407, 520
- Padmanabhan N., Schlegel D. J., Seljak U., Makarov A., Bahcall N. A., Blanton M. R., Brinkmann J., Eisenstein D. J., Finkbeiner D. P., Gunn J. E., and co-authors, 2007, *MNRAS*, 378, 852
- Peebles P. J. E., 1980, *The large-scale structure of the universe*. Princeton University Press, 1980
- Ross A. J., Percival W. J., Crocce M., Cabré A., Gaztañaga E., 2011, *MNRAS*, 415, 2193
- Scoccimarro R., Zaldarriaga M., Hui L., 1999, *Astrophys. J.*, 527, 1
- Smith R. E., 2009, *MNRAS*, 400, 851
- Smith R. E., Peacock J. A., Jenkins A., White S. D. M., Frenk C. S., Pearce F. R., Thomas P. A., Efstathiou G., Couchman H. M. P., 2003, *MNRAS*, 341, 1311
- Smith R. E., Reed D. S., Potter D., Marian L., Crocce M., Moore B., 2012, ArXiv e-prints
- Springel V., 2005, *MNRAS*, 364, 1105
- Takahashi R., Sato M., Nishimichi T., Taruya A., Oguri M., 2012, *Astrophys. J.*, 761, 152
- Takahashi R., Yoshida N., Takada M., Matsubara T., Sugiyama N., Kayo I., Nishizawa A. J., Nishimichi T., Saito S., Taruya A., 2009, *Astrophys. J.*, 700, 479
- Teyssier R., Pires S., Prunet S., Aubert D., Pichon C., Amara A., Benabed K., Colombi S., Refregier A., Starck J.-L., 2009, *A&A*, 497, 335
- Watson W. A., Diego J. M., Gottlöber S., Iliev I. T., Knebe A., Martínez-González E., Yepes G., Barreiro R. B., González-Nuevo J., Hotchkiss S., Marcos-Caballero A., Nadathur S., Vielva P., . 2013, ArXiv e-prints